A well-balanced lattice Boltzmann method based on quasi-incompressible phase-field theory*

LI Chunyi, GUO Zhaoli

State Key Laboratory of Coal Combustion, Huazhong University of Science and Technology, Wuhan 430074, China

Abstract

Compared with the lattice Boltzmann equation (LBE) model based on incompressible phase field theory, the LBE based on quasi-incompressible phase field theory has the advantage of local mass conservation. However, previous quasi-incompressible phase-field-based LBE model does not satisfy the well-balanced property, resulting in spurious velocities in the vicinity of interface and density profiles inconsistent with those from thermodynamics. To address this problem, a novel LBE model is developed based on the quasi-incompressible phase-field theory. First, numerical artifacts in the original LBE for the Cahn-Hilliard are analyzed. Based on this analysis, the equilibrium distribution function and source term are reformulated to eliminate the numerical artifacts, enabling the new LBE to realize the well-balanced characteristics at a discrete level. The performance of the proposed LBE model is tested by simulating a number of typical two-phase systems. The numerical results of the planar interface and static droplet problems demonstrate that the present model can eliminate spurious velocities and achieve well-balanced state. Numerical results of the layered Poiseuille flow demonstrate the accuracy of the present model in simulating dynamic two-phase flow problems. The well-balanced properties of the LBE model with two different formulations of surface tension ($\boldsymbol{F}_s = -\phi\nabla\mu$ and $\boldsymbol{F}_s = \mu\nabla\phi$) are also investigated. It is found that the formulation of $\boldsymbol{F}_s = \mu\nabla\phi$ cannot eliminate the spurious velocities, while the formulation of $\boldsymbol{F}_s = \mu\nabla\phi$ can achieve the well-balanced state. The influences of viscosity formulations of the fluid mixture are also compared. Particularly, four mixing rules are considered. It is shown that the use of step mixing rule gives more accurate results for the layered Poiseuille flow. Finally, we compare the performance of the present quasi-incompressible LBE model with that of the original fully incompressible LBE model by simulating the phase separation problem, and the results show that the present model can ensure the local mass conservation, while the fully incompressible LBE can yield quite different predictions.

---

* The paper is an English translated version of the original Chinese paper published in Acta Physica Sinica. Please cite the paper as: **LI Chunyi, GUO Zhaoli**. **A well-balanced lattice Boltzmann method based on quasi-incompressible phase-field theory**, Acta Phys. Sin., 2025, 74(6): 064702. doi: 10.7498/aps.74.20241513

Keywords: two-phase flow, lattice Boltzmann method, quasi-incompressible phase field model

PACS: 47.11.Qr, 47.61.Jd

doi: 10.7498/aps.74.20241513

cstr：32037.14.aps.74.20241513

1. Introduction

Lattice Boltzmann equation (LBE) method based on mesoscopic kinetic theory is an effective research method for multiphase flow simulation, and many effective LBE models have been developed[1-4]. However, the conventional multiphase LBE models still have some fundamental problems, such as inaccurate interface capture and spurious velocity. In theory, when the system reaches equilibrium, the chemical potential should be constant, and the fluid loses its driving force and its velocity should be zero. However, in the existing multi-phase LBE model, the spurious velocity near the interface cannot be completely eliminated[5-13]. In general, the spurious velocity is much smaller than the characteristic velocity of the problem, which has little effect on the simulation. However, in some cases, the spurious velocity can lead to numerical instability and unphysical phenomena. For example, the two-phase density distribution of the pseudo-potential model[7,8] can deviate significantly from the Maxwell's coexistence curve. Similar unphysical phenomena have been observed in the phase-field model[9].

Various attempts have been made to identify the source of the spurious velocity and mitigate its effects. For example, Cristea and Sofonea[10] identified that the reason for the spurious velocity in the finite-difference LBE models is the first-order upwind scheme for calculating the space derivatives in the evolution equation, and they introduced a correction force term to solve this problem. Wagner[11] attributed the spurious velocity to the discretizations of the driving forces, and demonstrated that using the potential form of the surface-tension force could eliminate spurious velocity. However, this approach introduced numerical instability, requiring additional stabilization terms dependent on numerical viscosity and velocity. Shan[12] identified the lack of isotropy in gradient-operator discretization within force terms as a key contributor to spurious velocity in pseudo-potential models. Building on this insight, Sbragaglia et al.[13] developed a high-order isotropic discretization scheme to reduce the spurious velocity of the pseudo-potential models.

Previous studies have shown that the spurious velocity of LBE comes from the spurious force

caused by the discretization errors. Guo et al.[14] conducted a rigorous mathematical analysis of the free energy LBE model and derived the total force imbalance equation. The results shown that the imbalance between the ideal gas pressure gradient and surface tension on the discrete level leads to spurious velocity. Subsequently, Guo[15] analyzed the structure of the unbalanced net force, and proposed a well-balanced (WB) LBE model that eliminates the spurious velocity entirely. Zhang et al.[16] proposed an improved model based on this to improve the numerical stability. Inspired by the WB-LBE model, Zheng et al.[17] proposed the treatment of the equilibrium forces in the phase field model, and established the phase field WB-LBE model by reconstructing the LBE corresponding to the Navier-Stokes equation. More recently, Ju et al.[18] demonstrated that the spurious velocity of the phase-field LBE model comes from the LBE solving the phase-field Cahn-Hilliard (CH) equation. They accordingly redesigned the corresponding LBE to establish another phase-field WB-LBE model.

The existing phase-field WB-LBE models have been proved to be able to eliminate the spurious velocity well. However, those models were developed based on the incompressible phase-field theory, and consequently failed to guarantee local mass conservation when the two fluids have different densities[19]. Subsequently, Yang and Guo[3] proposed a LBE model based on the quasi-incompressible phase field model[20], which achieves the local mass conservation, but still exhibits significant spurious velocity**.** Therefore, the purpose of this paper is to develop a WB-LBE model based on the quasi-incompressible phase field theory**.**

This paper is organized as follows. Section 2 briefly introduces the quasi-incompressible phase-field LBE model. In section3 we analyze the source of spurious velocity, propose a well-balanced LBE model, and verify its well-balanced property by Chapman-Enskog (CE) expansion. Section4 presents validation cases to demonstrate the model's performance. Finally, section5 concludes the paper**.**

2. LBE model based on quasi-incompressible phase field theory

2.1 Quasi-incompressible phase field theory

The phase-field theory describes the thermodynamic behavior of a two-phase system in terms of a free energy function, which can be represented by an order parameter ϕ labeling the fluids of different phases:

$$F(\phi) = \int_{\Omega} \left[\psi(\phi) + \frac{\kappa}{2} |\nabla \phi|^2 \right] \mathrm{d}\Omega, \qquad (1)$$

where $\psi(\phi)$ is the bulk free energy density, κ is the surface tension coefficient, and Ω is the control volume. For a two-phase system, the bulk free energy density can take the double-well

form[21]:

$$\psi(\phi) = \beta(\phi - \phi_1)^2(\phi - \phi_2)^2, \tag{2}$$

where ϕ_1 and ϕ_2 are the order parameters of phase 1 and phase 2, respectively, and in general, $\phi_1 = 1$ and $\phi_2 = 0$. β is a constant related to κ, and they satisfy the following relations:

$$\sigma = \frac{|\phi_1 - \phi_2|^3}{6}\sqrt{2\kappa\beta}, \tag{3}$$

$$W = \frac{1}{|\phi_1 - \phi_2|}\sqrt{\frac{8\kappa}{\beta}}, \tag{4}$$

where σ is the surface tension and W represents the interface thickness. The chemical potential μ can be obtained in terms of the free energy function, i.e.

$$\begin{aligned} \mu &= \frac{\delta F(\phi)}{\delta\phi} = \frac{\partial\psi}{\partial\phi} - \kappa\nabla^2\phi \\ &= 4\beta(\phi - \phi_1)(\phi - \phi_2)\left(\phi - \frac{\phi_1 + \phi_2}{2}\right) - \kappa\nabla^2\phi. \end{aligned} \tag{5}$$

The evolution of the order parameter satisfies the Cahn-Hilliard (CH) equation:

$$\partial_t\phi + \nabla\cdot(\phi\boldsymbol{u}) = \nabla\cdot(\lambda\nabla\mu), \tag{6}$$

where $\boldsymbol{u}$ is the fluid velocity and λ is the mobility coefficient.

In incompressible phase-field theory, the governing equations describing the fluid also include the incompressible Navier-Stokes (NS) equation:

$$\nabla\cdot\boldsymbol{u} = 0, \tag{7}$$

$$\begin{aligned} &\partial_t(\rho\boldsymbol{u}) + \nabla\cdot(\rho\boldsymbol{u}\boldsymbol{u}) \\ &= -\nabla p + \nabla\cdot\left\{\rho\nu\left[\nabla\boldsymbol{u} + (\nabla\boldsymbol{u})^{\mathrm{T}}\right]\right\} + \boldsymbol{F}, \end{aligned} \tag{8}$$

where p is the kinetic pressure; $\boldsymbol{F} = \boldsymbol{F}_s + \boldsymbol{G}$ is the total force, including surface tension $\boldsymbol{F}_s$ and external body force $\boldsymbol{G}$. Zhang et al. [4] pointed out that when the surface tension is in the form of potential energy, the smaller spurious velocity could be obtained. Therefore, unless

otherwise specified, the surface tension in the form of $\boldsymbol{F}_s = -\phi\nabla\mu$ is used in our simulations, and the gradient operator is discretized using an isotropic central difference scheme (41). ρ and ν are the density and kinematic viscosity of the mixed fluid, respectively, which can be expressed by the linear mixing rule as

$$\rho = \frac{\phi - \phi_2}{\phi_1 - \phi_2}\rho_1 + \frac{\phi_1 - \phi}{\phi_1 - \phi_2}\rho_2, \tag{9a}$$

$$\rho\nu = \frac{\phi - \phi_2}{\phi_1 - \phi_2}\rho_1\nu_1 + \frac{\phi_1 - \phi}{\phi_1 - \phi_2}\rho_2\nu_2, \tag{9b}$$

where ρ_1 and ρ_2 represent the densities of phase 1 and phase 2, respectively, and ν_1 and ν_2 represent the kinematic viscosities of phase 1 and phase 2, respectively. Since the actual physical meaning of ϕ is the volume fraction of phase 1, according to the definition of density, the mixing density is generally calculated by the linear mixing rule, while the viscosity can be calculated by different mixing rules, such as the reciprocal rule, the exponential rule and the step rule, which will be compared later. The above model has been widely used in the field of multiphase flow. However, substituting (7) and (9a) into (6) gives:

$$\partial_t\rho + \nabla\cdot(\rho\boldsymbol{u}) = \frac{\rho_1 - \rho_2}{\phi_1 - \phi_2}\nabla\cdot(\lambda\nabla\mu). \tag{10}$$

Obviously, when $\rho_1 \neq \rho_2$, the incompressible phase field model cannot guarantee local mass conservation.

The quasi-incompressible phase-field model[20] no longer assumes that the velocity divergence is 0, but takes

$$\nabla\cdot\boldsymbol{u} = -\gamma\nabla\cdot(\lambda\nabla\mu) \tag{11}$$

where γ is a coefficient related to the density of the two phases, which can be expressed as

$$\gamma = \frac{\rho_1 - \rho_2}{\phi_1\rho_2 - \phi_2\rho_1}. \tag{12}$$

Substituting (9), (11) and (12) into (6), we can get:

$$\partial_t\rho + \nabla\cdot(\rho\boldsymbol{u}) = 0. \tag{13}$$

This shows that the quasi-incompressible phase-field model strictly satisfies the local mass conservation.

2.2 Quasi-incompressible phase-field LBE model.

Yang and Guo[3] proposed the corresponding LBE model based on the quasi-incompressible phase-field theory. Two LBEs are used to describe the flow and phase field respectively. The LBEs for solving the NS equation and the CH equation are

$$\begin{aligned} & f_i\left(\boldsymbol{x}+\boldsymbol{e}_i\delta_t, t+\delta_t\right)-f_i\left(\boldsymbol{x}, t\right) \\ = & -\frac{1}{\tau_f}\left[f_i\left(\boldsymbol{x}, t\right)-f_i^{\mathrm{eq}}\left(\boldsymbol{x}, t\right)\right] \\ & +\delta_t\left[1-\frac{1}{2\tau_f}\right] F_i\left(\boldsymbol{x}, t\right), \end{aligned} \tag{14}$$

$$\begin{aligned} & g_i\left(\boldsymbol{x}+\boldsymbol{e}_i\delta_t, t+\delta_t\right)-g_i\left(\boldsymbol{x}, t\right) \\ = & -\frac{1}{\tau_g}\left[g_i\left(\boldsymbol{x}, t\right)-g_i^{\mathrm{eq}}\left(\boldsymbol{x}, t\right)\right] \\ & +\delta_t\left[1-\frac{1}{2\tau_g}\right] G_i\left(\boldsymbol{x}, t\right), \end{aligned} \tag{15}$$

where $f_i(\boldsymbol{x}, t)$ and $g_i(\boldsymbol{x}, t)$ represent the distribution function in the direction of i located at x at the time of t, which are the pressure distribution function and the order parameter distribution function, respectively; τ_f and τ_g are the dimensionless relaxation times associated with viscosity and mobility coefficient, respectively; f_i^{eq} and g_i^{eq} are equilibrium distribution functions defined as

$$f_i^{\mathrm{eq}}=\omega_i\left[p+c_{\mathrm{s}}^2 \rho s_i\left(\boldsymbol{u}\right)\right], \tag{16}$$

$$g_i^{\mathrm{eq}}=\omega_i \phi s_i\left(\boldsymbol{u}\right)+\begin{cases}\phi+\left(\omega_i-1\right)\alpha\mu, & i=0 \\ \omega_i \alpha\mu, & i\neq 0\end{cases}, \tag{17}$$

with

$$s_i\left(\boldsymbol{u}\right)=\frac{\boldsymbol{e}_i\cdot\boldsymbol{u}}{c_{\mathrm{s}}^2}+\frac{\boldsymbol{u}\boldsymbol{u}:\left(\boldsymbol{e}_i\boldsymbol{e}_i-c_{\mathrm{s}}^2\boldsymbol{I}\right)}{2c_{\mathrm{s}}^4}. \tag{18}$$

Here α is an adjustable parameter, which is generally taken as 1; $c_{\mathrm{s}}=c/\sqrt{3}$ is the lattice sound speed; The ω_i is the weighting coefficient; $\boldsymbol{e}_i$ is the ith discrete velocity. Taking the D2Q9 model as an example, the weighting coefficients are $\omega_0=4/9,\ \omega_{1-4}=1/$

9 and $\omega_{5-8} = 1/36$, and the discrete velocities are $\boldsymbol{e}_0 = (0,0)$, $\boldsymbol{e}_{1-4} = c\{\cos[(\mathrm{i}-1)\pi/2], \sin[(\mathrm{i}-1)\pi/2]\}$ and $\boldsymbol{e}_{5-8} = \sqrt{2}c\{\cos[(2\mathrm{i}-1)\pi/4], \sin[(2\mathrm{i}-1)\pi/4]\}$, where $c = \delta_x/\delta_t$, while δ_x and δ_t are the space step and time step, respectively. F_i and G_i are source terms defined as

$$F_i = (\boldsymbol{e}_i - \boldsymbol{u}) \cdot [\omega_i \boldsymbol{F}\,[1 + s_i\,(\boldsymbol{u})] + \omega_i s_i\,(\boldsymbol{u})\, c_\mathrm{s}^2 \nabla\rho] - \omega_\alpha c_\mathrm{s}^2 \rho\gamma\nabla \cdot (\lambda\nabla\mu), \tag{19}$$

$$G_i = -\frac{\omega_i \phi}{c_\mathrm{s}^2 \rho}(\boldsymbol{e}_i - \boldsymbol{u}) \cdot (\nabla p - \boldsymbol{F})\,[1 + s_i\,(\boldsymbol{u})]\,. \tag{20}$$

The macroscopic quantities include pressure p, velocity $\boldsymbol{u}$ and order parameter ϕ, which can be statistically obtained by

$$p = \sum\nolimits_i f_i + \frac{\delta t}{2} c_\mathrm{s}^2 (\boldsymbol{u} \cdot \nabla\rho - \gamma\rho\nabla \cdot (\lambda\nabla\boldsymbol{\mu}))\,, \tag{21}$$

$$\boldsymbol{u} = \frac{1}{c_\mathrm{s}^2 \rho}\left[\sum\nolimits_i \boldsymbol{e}_i f_i + \frac{\delta t}{2} c_\mathrm{s}^2 \boldsymbol{F}\right], \tag{22}$$

$$\phi = \sum\nolimits_i g_i\,. \tag{23}$$

Through Chapman-Enskog (CE) expansion, the model can recover the macroscopic equation, and the calculation formulas of kinematic viscosity and mobility coefficient are obtained:

$$\nu = c_\mathrm{s}^2\,(\tau_f - 0.5)\,\delta_t, \tag{24}$$

$$\lambda = c_\mathrm{s}^2 \alpha\,(\tau_g - 0.5)\,\delta_t. \tag{25}$$

For convenience, we call the above LBE model the YG-LBE model.

3. A well-balanced LBE model based on quasi-incompressible phase-field theory

3.1 The source of the spurious velocity

Similar to most two-phase LBE models, the YG-LBE model also has the spurious velocity. Ju et al.[18] analysis found that the root cause is that the equilibrium function and source term in the LBE solving the CH equation are not in balance at the discrete level. The macroscopic equation recovered by the YG-LBE model through the CE expansion is [18].

$$\partial_t \phi + \nabla \cdot (\phi \boldsymbol{u}) = \lambda \nabla \cdot (\nabla \mu + \Gamma_1 - \Gamma_2), \tag{26}$$

with

$$\Gamma_1 = \partial_{t1} (\phi \boldsymbol{u}) + \nabla \cdot (\phi \boldsymbol{u}\boldsymbol{u}) = \frac{\phi}{\rho}(\boldsymbol{F} - \nabla p), \tag{27}$$

$$\Gamma_2 = \sum\nolimits_i \boldsymbol{e}_i G_i^{(0)} = \frac{\phi}{\rho}(\boldsymbol{F} - \nabla p). \tag{28}$$

Obviously, the expressions for Γ_1 and Γ_2 are the same, and in general, they can be considered to cancel each other. However, the Γ_1 arises from the collision and stream of the LBE and originates from the equilibrium distribution function; The Γ_2 is an additional term in the source term in order to eliminate Γ_1. However, they are essentially from different sources, and their discrete templates are different on the numerical grid, so they would produce non-zero chemical potential gradients, which would lead to the emergence of spurious velocity.

3.2 The well-balanced LBE model.

The above analysis shows that the origin of the Γ_1 and Γ_2 lies in the fact that the equilibrium distribution function (17) introduces a $s_i(\boldsymbol{u})$ to recover the convective term $\nabla \cdot (\phi \boldsymbol{u})$ in the CH equation. The $s_i(\boldsymbol{u})$ leads to the appearance of Γ_1, so the artificial term Γ_2 needs to be introduced to offset it. The solution is to[18] remove the $s_i(\boldsymbol{u})$ from the equilibrium distribution function and restore the exact convective term by redesigning the source term. In this way, Γ_1 no longer appears, and the artificial term Γ_2 is no longer needed. Based on the above idea, we redesign the LBE for solving the CH equation and develop an well-balanced model based on the quasi-incompressible phase-field theory.

The new LBE for solving the CH equation is[22]

$$\begin{aligned} & g_i(\boldsymbol{x} + \boldsymbol{e}_i \delta_t, t + \delta_t) - g_i(\boldsymbol{x}, t) \\ = & -\frac{1}{\tau_g}[g_i(\boldsymbol{x}, t) - g_i^{\mathrm{eq}}(\boldsymbol{x}, t)] + \delta_t G_i(\boldsymbol{x}, t) \\ & + \frac{\delta_t^2}{2} \partial_t G_i(\boldsymbol{x}, t), \end{aligned} \tag{29}$$

where the equilibrium distribution function no longer contains $s_i(\boldsymbol{u})$ and is defined as

$$g_i^{\mathrm{eq}} = \begin{cases} \phi + (\omega_i - 1)\,\alpha\mu, & i = 0, \\ \omega_i \alpha \mu, & i \neq 0. \end{cases} \tag{30}$$

In order to accurately recover the CH equation, the new source term is defined as

$$G_i = \omega_i \left[\nabla \cdot (\phi \boldsymbol{u})\right] \left[-1 + \frac{\boldsymbol{I} : (\boldsymbol{e}_i \boldsymbol{e}_i - c_{\mathrm{s}}^2 \boldsymbol{I})}{2c_{\mathrm{s}}^2}\right]. \tag{31}$$

The order parameter is calculated as

$$\phi = \sum\nolimits_i g_i \,. \tag{32}$$

In order to analyze the macroscopic equation corresponding to the LBE (29), the CE analysis is carried out. First, the following multi-scale expansions is introduced:

$$g_i = g_i^{(0)} + \varepsilon g_i^{(1)} + \varepsilon^2 g_i^{(2)} + \cdots, \tag{33}$$

$$\partial_t = \varepsilon \partial_{t0} + \varepsilon^2 \partial_{t1}, \ \nabla = \varepsilon \nabla_0, \ G_i = \varepsilon G_i^{(0)}. \tag{34}$$

Applying Taylor expansion to (29), one obtains:

$$D_i g_i + \frac{\delta_t}{2} D_i^2 g_i = -\frac{1}{\delta_t \tau_g}(g_i - g_i^{\mathrm{eq}}) + G_i + \frac{\delta_t}{2} G_i, \tag{35}$$

where $D_i = \partial_t + \boldsymbol{e}_i \cdot \nabla$. Substituting (33) and (34) into (35), the equations on different scales can be obtained:

$$O\left(\varepsilon^0\right) : g_i^{(0)} = g_i^{\mathrm{eq}}, \tag{36a}$$

$$O\left(\varepsilon^1\right) : D_{i0} g_i^{(0)} = -\frac{1}{\delta_t \tau_g} g_i^{(1)} + G_i^{(0)}, \tag{36b}$$

$$\begin{aligned} &O\left(\varepsilon^2\right) : \partial_{t1} g_i^{(0)} + D_{i0} g_i^{(1)} + \frac{\delta_t}{2} D_{i0}^2 g_i^{(0)} \\ &= -\frac{1}{\delta_t \tau_g} g_i^{(2)} + \frac{\delta_t}{2} \partial_{t0} G_i^{(0)}. \end{aligned} \tag{36c}$$

According to (36b), the equation (36c) can be written as

$$\partial_{t1} g_i^{(0)} + \left(1 - \frac{1}{2\tau_g}\right) D_{i0} g_i^{(1)} + \frac{\delta_t}{2} \boldsymbol{e}_i \cdot \nabla_0 G_i^{(0)} = -\frac{1}{\delta_t \tau_g} g_i^{(2)}. \tag{37}$$

According to the definition of the equilibrium distribution function g_i^{eq} and the source term G_i, some velocity moments can be obtained as follows:

$$\sum\nolimits_i g_i^{(0)} = \phi,\ \sum\nolimits_i \boldsymbol{e}_i g_i^{(0)} = 0,\ \sum\nolimits_i \boldsymbol{e}_i \boldsymbol{e}_i g_i^{(0)} = c_{\mathrm{s}}^2 \alpha \mu \boldsymbol{I}, \tag{38a}$$

$$\sum\nolimits_i g_i^{(1)} = \sum\nolimits_i g_i^{(2)} = 0,\ \ \sum\nolimits_i \boldsymbol{e}_i g_i^{(1)} = -\delta_t \tau_g c_{\mathrm{s}}^2 \alpha \nabla \mu, \tag{38b}$$

$$\sum\nolimits_i G_i^{(0)} = -\nabla_0 \cdot (\phi \boldsymbol{u}),\ \ \sum\nolimits_i \boldsymbol{e}_i G_i^{(0)} = 0, \tag{38c}$$

Taking the zeroth-order moment of (36b) and (37) and using (38), we can get:

$$\partial_{t0} \phi + \nabla_0 \cdot (\phi \boldsymbol{u}) = 0, \tag{39a}$$

$$\partial_{t1} \phi = \nabla_0 \cdot \left[c_{\mathrm{s}}^2 \alpha \delta_t \left(\tau_g - 0.5\right) \nabla_0 \mu\right]. \tag{39b}$$

Combining (39a) and (39b), the following CH equation is obtained:

$$\partial_t \phi + \nabla \cdot (\phi \boldsymbol{u}) = \nabla \cdot (\lambda \nabla \mu). \tag{40}$$

From the above derivation, it can be seen that the current model avoids the generation of the unbalanced term in the process of recovering the macroscopic equation, and can achieve accurate balance on the discrete level.

In order to facilitate the calculation and ensure the second-order spatial accuracy, the isotropic central difference scheme is used to discretize the gradient operator and Laplace operator:

$$\nabla \phi = \frac{1}{c_{\mathrm{s}}^2 \delta_t} \sum \omega_i \boldsymbol{e}_i \phi(\boldsymbol{x} + \boldsymbol{e}_i \delta_t), \tag{41a}$$

$$\nabla^2 \phi = \frac{2}{c_{\mathrm{s}}^2 \delta_t} \sum \omega_i \left[\phi\left(\boldsymbol{x} + \boldsymbol{e}_i \delta_t\right) - \phi\left(\boldsymbol{x}\right)\right], \tag{41b}$$

where ϕ can be any physical quantity.

For convenience, the model is called well-balanced (WB) -LBE model in this paper.

4. Numerical verification

In this section, several typical examples will be simulated to verify the performance of WB-LBE and compare with YG-LBE model.

4.1 Flat interface problem

Firstly, a flat interface problem in x-y coordinate system is simulated. The computational domain is a rectangular area of size $L_x \times L_y = 30 \times 128$, where L_x and L_y are the width and height of the domain, respectively. The computational grid is $N_x \times N_y = 30 \times 128$. At the beginning, the phase 1 is distributed in the central area, and the rest space is filled with the phase 2. The initial order parameter is set according to:

$$\phi_0 = \phi_2 + 0.5\,(\phi_1 - \phi_2)\left[\tanh\left(2\frac{y - y_1}{W}\right) + \tanh\left(2\frac{y - y_2}{W}\right)\right], \tag{42}$$

where $y_1 = N_y/4$ and $y_2 = 3N_y/4$ are the lower and upper boundaries of the region where the phase 1 is located, respectively; W is the interface thickness, which is set as $W = 4$ in this paper. In the simulation, all four boundaries are set as periodic boundaries. The density and kinematic viscosity of the phase 1 are $\rho_1 = 10$ and $\nu_1 = 0.1$, respectively, while the density and kinematic viscosity of the phase 2 are $\rho_2 = 1.0$ and $\nu_2 = 0.1$, respectively; the surface tension is $\sigma = 0.005$, and the mobility coefficient is $\lambda = 0.1$.

For the sake of comparison, we characterize the magnitude of the spurious velocity by the total kinetic energy of the system, E, which is defined as

$$E = \frac{1}{2}\int_{\Omega} \rho |\boldsymbol{u}|^2 \mathrm{d}\boldsymbol{x}, \tag{43}$$

where Ω denotes the computational domain. The results of WB-LBE and YG-LBE are given by Fig. 1. The Fig. 1(a) gives the evolution of the total kinetic energy E with time step t. It can be seen from the Fig. 1(a) that before about $t = 10^6$, the total kinetic energy of the two has the same change trend, which first decreases to the order of about 10^{-15} with time, then increases to the order of about 10^{-5}, and then begins to decrease gradually with time. However, after some time between $t = 10^6$—$10^{6.5}$, the total kinetic energy of the YG-LBE

rises rapidly again until the numerical divergence while the total kinetic energy of WB-LBE decreases continuously and finally stabilizes at the order of about 10^{-25}. The velocity distribution of WB-LBE in steady state is given by Fig. 1(b). From Fig. 1(b), it can be found that the spurious velocity is in the order of 10^{-15}, reaching machine precision. The maximum spurious velocity of YG-LBE is still in the order of 10^{-9} even at the time when the total kinetic energy decreases to the minimum (Fig. 1(c)). The chemical potential distributions obtained by the two models when the total kinetic energy reaches its minimum are given by Fig. 1(d) . It can be seen that the chemical potential of the YG-LBE model has a change of the order of 10^{-8}, while the chemical potential of the present model is basically constant, and its change is of the order of 10^{-15}.

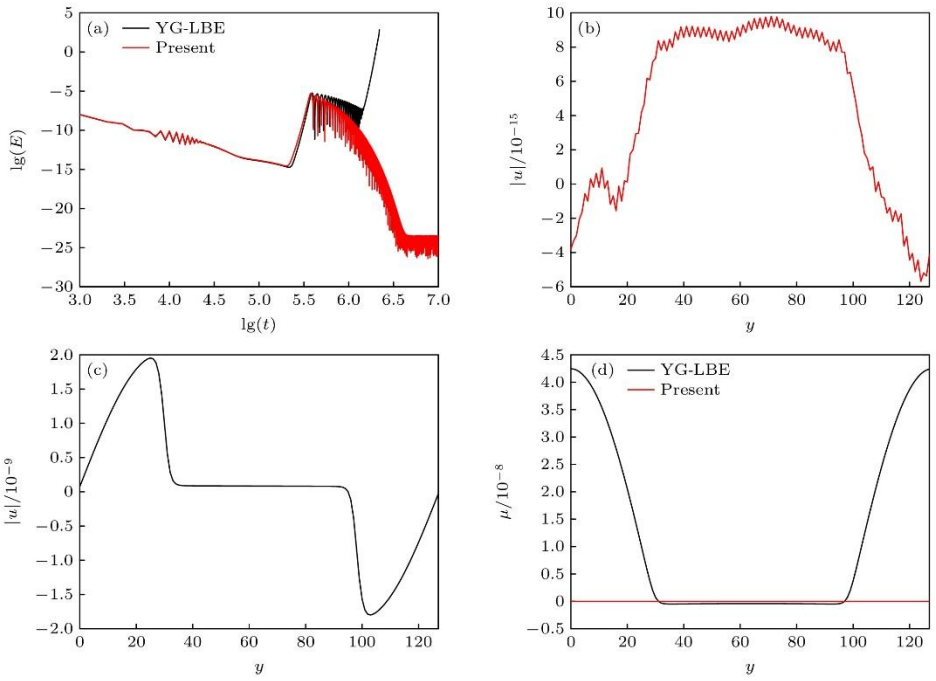

Figure 1. Numerical results of the WB-LBE and YG-LBE models for the planar interface: (a) Time evolution of the total kinetic energy; (b) distribution of velocity obtained by the WB-LBE model at steady state; (c) distribution of velocity obtained by the YG-LBE model at steady state; (d) distributions of chemical potential.

4.2 Stationary droplet problem

We further simulate a two-dimensional stationary droplet problem. The droplet radius is *R*, and the size of computational domain is $N_x \times N_y = 128 \times 128$. The droplet is represented by the phase 1, with radius $R = N_x/4$, initially placed in the center of the computational domain, and filled with the phase 2 elsewhere. The order parameter is initialized as

$$\phi = \frac{\phi_1 + \phi_2}{2} + \frac{\phi_1 - \phi_2}{2} \times \tanh\left[2\frac{R - \sqrt{(x - x_c)^2 + (y - y_c)^2}}{W}\right], \tag{44}$$

where $(x_c, y_c) = (N_x/2, N_y/2)$ is the coordinate of the initial position of the center of the droplet. In the simulation, periodic boundaries are used for all four boundaries, and other parameters are the same as those of the flat interface problem mentioned above.

We compare the results of the WB-LBE model and the YG-LBE model in this paper, as shown in Fig. 2. The time evolution process of the total kinetic energy given by the Fig. 2(a) is different from that of the flat interface problem, which is no longer a stage of first decreasing and then increasing rapidly, but a nearly monotonous decreasing process. Similar to the flat interface problem, after a certain time between $t = 10^6$—$10^{6.5}$, the *E* in the results of the YG-LBE model increases rapidly with time until it stabilizes at the order of 10^2, when the spurious velocity is extremely large. The total kinetic energy *E* calculated by the WB-LBE model decreases with time and finally stabilizes at the order of about 10^{-25}. From the velocity distribution given by Fig. 2(b), it can be seen that the spurious velocity is in the order of 10^{-15}, reaching machine accuracy. When the *E* is the lowest, the spurious velocity of the YG-LBE model shown by Fig. 2(c) is still in the order of 10^{-8}. From the chemical potential distribution given by Fig. 2(d), it can also be found that when *E* reaches the minimum, the chemical potential of YG-LBE model changes by the order of 10^{-7}, while the chemical potential of WB-LBE model remains basically constant. The above comparisons show that the current model can achieve an well-balanced state.

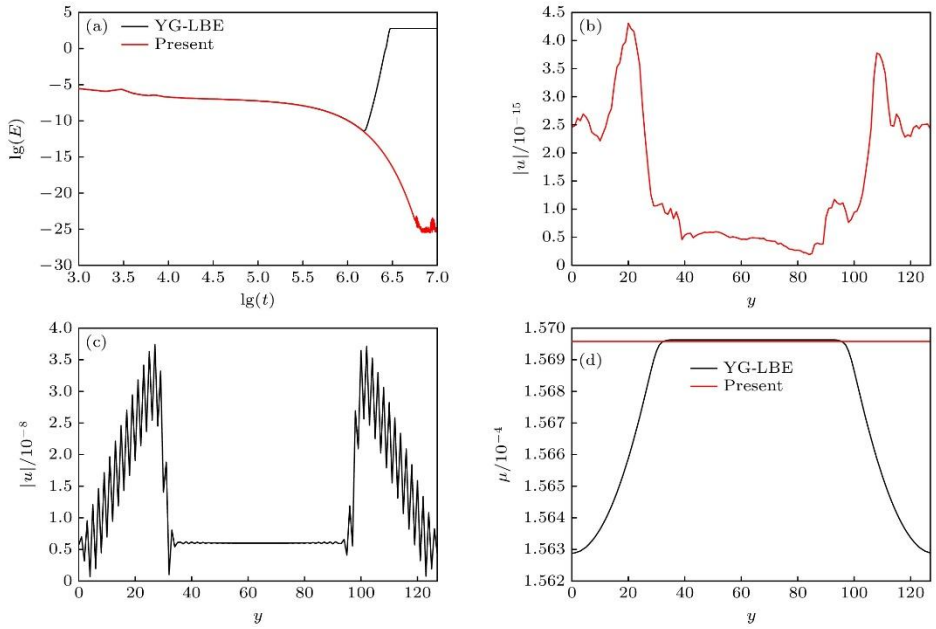

Figure 2. Results of the WB-LBE and YG-LBE models for the steady-state droplet problem: (a) Time evolution of the total kinetic energy; (b) velocity distribution obtained by the WB-LBE model; (c) velocity distribution obtained by the YG-LBE model; (d) distributions of chemical potential.

In the following, we compare the effects of two forms of surface tension on the performance of the model. The expressions for these two forms of surface tension are[4]:

$$\boldsymbol{F}_{\mathrm{s}} = -\phi\nabla\mu, \tag{45a}$$

$$\boldsymbol{F}_{\mathrm{s}} = \mu\nabla\phi. \tag{45b}$$

The results are shown in Fig. 3, where case1 and case2 used the (45a) and (45b) equations, respectively, to calculate the surface tension. The time evolution of the total kinetic energy in two cases is given by the Fig. 3(a). From the Fig. 3(a), it can be seen that the total kinetic energy in case1 decreases to the order of 10^{-25}, while the total kinetic energy in case2 increases suddenly in the middle and finally stabilizes at a higher level. This shows that the use of surface tension in the form of (45b) cannot eliminate the spurious velocity. The surface tension of (45a) and (45b) are usually considered to be equivalent, but in equilibrium, (45b) can not guarantee that the chemical potential is constant, so it can not achieve well-balanced state. The chemical potential distribution in two cases is given by Fig. 3(b). It can be seen that the chemical potential in case1 is constant, while the chemical potential in case2 changes obviously.

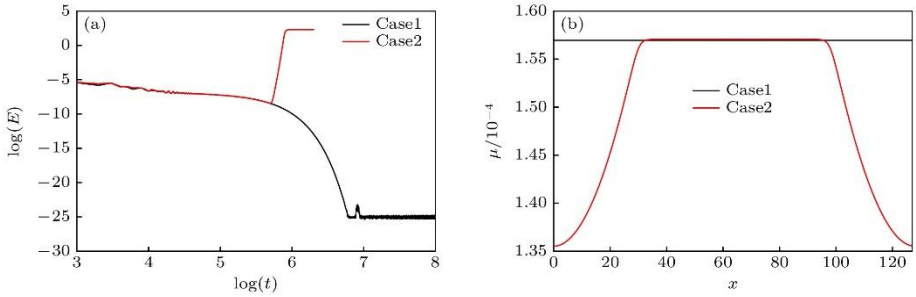

Figure 3. Numerical results of the steady-state droplet problem using different forms of surface tension: (a) Time evolution of the total kinetic energy; (b) distributions of chemical potential.

The above simulations all use the linear viscosity mixing rule. As mentioned earlier, the viscosity mixing rule also includes the reciprocal rule, the exponential rule, and the step rule, which are

$$\frac{1}{\rho\nu} = \frac{\phi}{\rho_1\nu_1} + \frac{1-\phi}{\rho_2\nu_2}, \tag{46a}$$

$$\ln(\rho\nu) = \phi\ln(\rho_1\nu_1) + (1-\phi)\ln(\rho_2\nu_2), \tag{46b}$$

$$\rho\nu = \begin{cases} \rho_1\nu_1, & \phi \geqslant 0.5, \\ \rho_2\nu_2, & \phi < 0.5. \end{cases} \tag{46c}$$

In order to compare their effects on the performance of the model, we increased the viscosity ratio, let $\nu_1 = 0.1,\ \nu_2 = 0.01$, and kept the other parameters. The results of different mixing rules are compared in Fig. 4, in which case1-case4 used (9b), (46a), (46b) and (46c) to calculate the mixing viscosity, respectively. From the Fig. 4(a), it can be seen that the order parameter distributions in the four cases are completely consistent, indicating that different viscosity mixing rules have no significant effect on the interface capturing performance of this problem. The distribution of chemical potential is given by Fig. 4(b). It can be seen that the chemical potential of the four cases is also constant and equal to the same value. Fig. 4(c) and (d) show the time evolution of the total kinetic energy and its partial magnification. It can be seen that different viscosity mixing rules show some differences in terms of spurious velocity. The total kinetic energy of case1 and case4 finally stabilizes at the order of 10^{-25} and 10^{-23}, respectively, and the total kinetic energy of case2 and case3 finally fluctuates between the order of 10^{-25} and 10^{-23}.

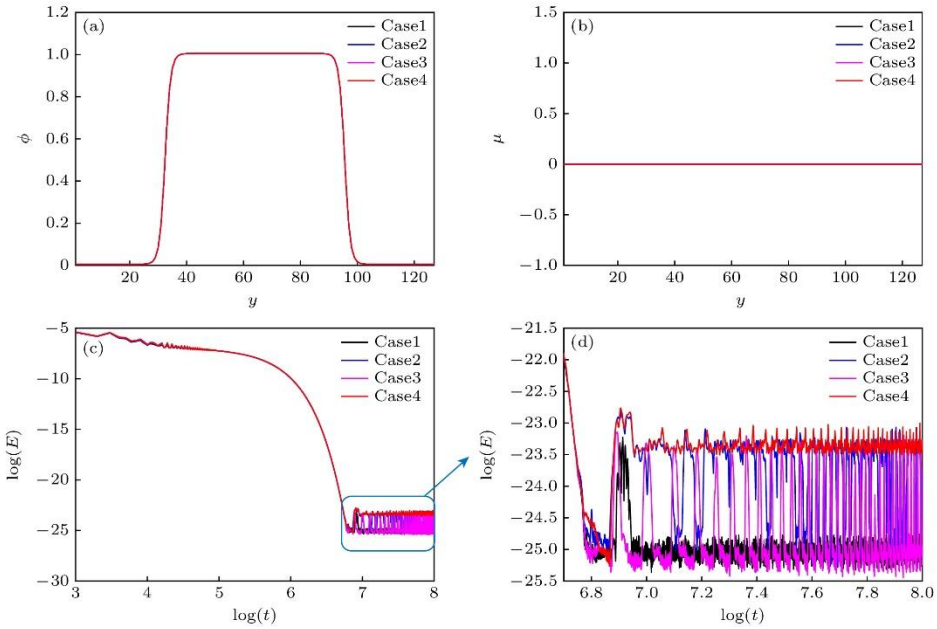

Figure 4. Numerical results of the steady-state droplet problem using different viscosity mixing rules: (a) Distributions of order parameter; (b) distributions of chemical potential; (c), (d) time evolution of total kinetic energy.

4.3 Layered Poiseuille flow

In this section, the problem of layered Poiseuille flow is simulated. The computational domain is set to $N_x \times N_y = 64 \times 250$, the upper and lower boundaries are no-slip solid boundaries, the modified bounce-back scheme is used to achieve no-slip boundaries, and the left and right boundaries are periodic boundaries. The upper part of the computational domain is filled with the phase 1 and the lower part with the phase 2. The flow is driven by a constant external force $G_x = 10^{-7}$ in the direction of the *x*. In the simulation, the density of the two phases is set as $\rho_1 = \rho_2 = 1.0$, the kinematic viscosity is $\nu_1 = 1.0$ and $\nu_2 = 0.1$, the surface tension is $\sigma = 0.005$, the mobility coefficient is $\lambda = 0.1$, and the interface thickness is $W = 4.0$. There exists an analytical solution for the distribution of the *x* direction velocity along the *y* direction for this problem:

$$u = \begin{cases} \dfrac{G_x h^2}{2\rho_2\nu_2}\left[-\left(\dfrac{y}{h}\right)^2 - \dfrac{y}{h}\dfrac{\rho_1\nu_1 - \rho_2\nu_2}{\rho_1\nu_1 + \rho_2\nu_2} + \dfrac{2\rho_2\nu_2}{\rho_1\nu_1 + \rho_2\nu_2}\right], & -h \leqslant y \leqslant 0, \\ \dfrac{G_x h^2}{2\rho_1\nu_1}\left[-\left(\dfrac{y}{h}\right)^2 - \dfrac{y}{h}\dfrac{\rho_1\nu_1 - \rho_2\nu_2}{\rho_1\nu_1 + \rho_2\nu_2} + \dfrac{2\rho_1\nu_1}{\rho_1\nu_1 + \rho_2\nu_2}\right], & 0 < y \leqslant h, \end{cases} \tag{47}$$

where $h = 124.5$ according to the number of grids we have taken.

In Section 4.2, we compared the effects of different viscosity mixing rules on the stationary

droplet problem, and we will further compare the differences between them by simulating the dynamic problem. The Fig. 5 shows the distribution of the velocity in the direction of the *x* along the direction of the *y* and its local amplification. Case1-4 use (9b), (46a), (46b) and (46c) to calculate the mixing viscosity, respectively. On the whole, the results of case2 and case4 are in good agreement with the analytical solution, and near the interface, the results of case4 are more consistent with the analytical solution. Therefore, when simulating dynamic problems, the step mixing rule of (46c) can be used to calculate the mixing viscosity to obtain more accurate results.

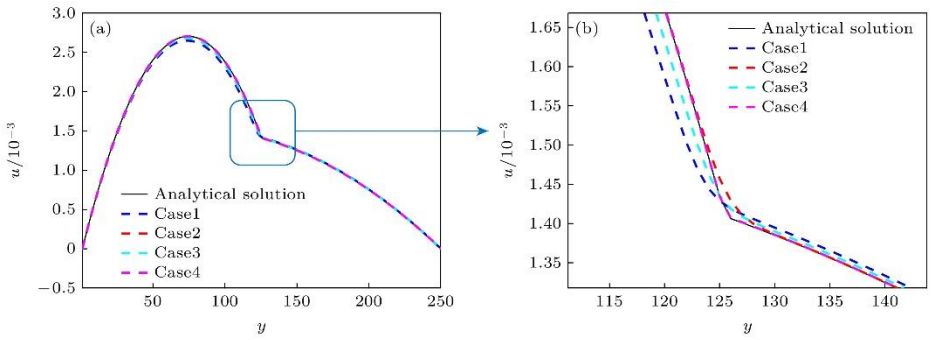

Figure 5. Distributions of flow velocity of the layered Poiseuille flow with different viscosity mixing rules.

In order to further verify the accuracy of the current model, the cases of different dynamic viscosity ratios $M = \frac{\mu_1}{\mu_2} = \frac{\rho_1 \nu_1}{\rho_2 \nu_2}$ are also simulated. We use the equation (46c) to calculate the viscosity of the mixture, set the density of the two phases to be $\rho_1 = \rho_2 = 1.0$, fix the $\nu_1 = 1.0$, and change the dynamic viscosity ratio by adjusting the value of ν_2. The Fig. 6 gives the velocity distribution for *M* = 10, 100, 1000, and the simulation results are in good agreement with the analytical solution. This demonstrates the accuracy of the current model in simulating dynamic problems and problems with large viscosity ratios.

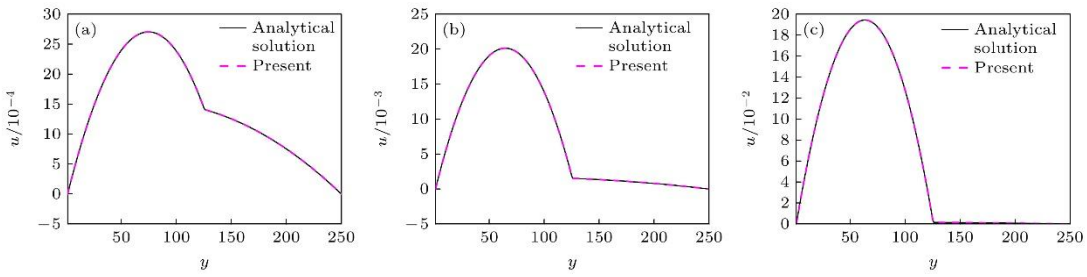

Figure 6. Distributions of flow velocity of the layered Poiseuille flow with different dynamic viscosity ratios: (a) *M*=10; (b) *M*=100; (c) *M*=1000.

4.4 Two-phase separation problem

In this section, a two-phase separation problem is simulated and compared with the LBE model[18] based on the incompressible phase-field theory. The calculation domain is a square area with a size of $N_x \times N_y = 100 \times 100$, and the initial timing parameters include a small perturbation, that is:

$$\phi = \frac{1}{2}\left[1 + 0.1\sin\left(\frac{4\pi x}{N_x}\right)\cos\left(\frac{4\pi y}{N_y}\right)\right]. \qquad (48)$$

In the simulation, the viscosity ratio $\nu_1/\nu_2 = 1$, the surface tension $\sigma = 0.001$, the relaxation time $\tau_f = \tau_g = 1.0$, and the interface thickness are set as $W = 4$.

In the LBE model[18] based on the incompressible phase-field theory, the corresponding continuity equation is (7). Compared with the quasi-incompressible continuity equation (11), the main difference between them is the right-hand term $\gamma\nabla\cdot(\lambda\nabla\mu)$, which is related to the parameter γ and only plays a role in the interface region. Therefore, when $\gamma = 0$ or in the bulk region, the two models are the same. When the γ is large or the proportion of the interface in the total area is large, the role of this term is greater, and the model difference will be obvious. In this example, we take $\gamma = 4$ and the density ratio is $\rho_1/\rho_2 = 5$ At the same time, the prediction results of the two models may be quite different because there are many two-phase interfaces at the initial time.

The Fig. 7 gives the phase distributions of the two models at different times, and it can be seen that the two models show great differences in phase separation. On the one hand, the results of the quasi-incompressible model evolve faster, and the predicted phase separation is earlier than that of the incompressible model; On the other hand, the two models obtain opposite results of phase separation. In the results of the quasi-incompressible model, the yellow phase is the discrete phase and the blue phase is the continuous phase, while the results of the incompressible model are just opposite.

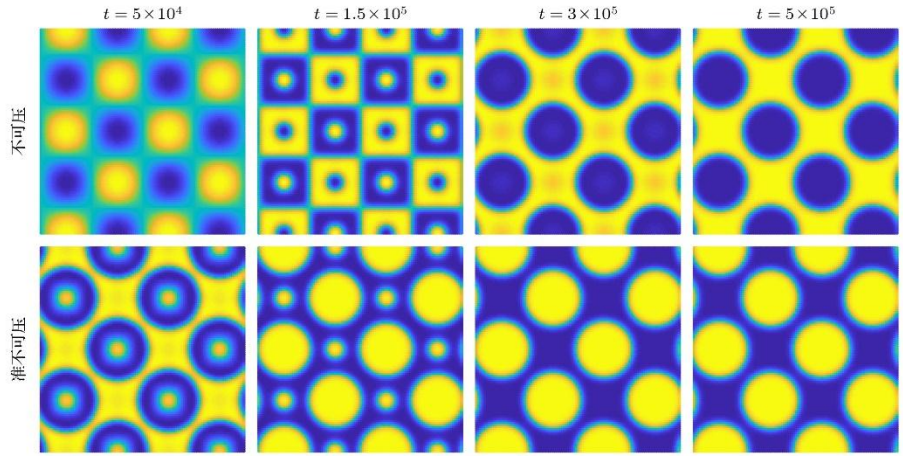

Figure 7. Phase distributions predicted by the incompressible model and the quasi-incompressible model. Yellow, Fluid 1; Blue, Fluid 2

We also count the mass changes of the two phases in this process, and calculate the total mass of the single phase at each time by the following formula:

$$m_1(t) = \int_{\Omega,\phi(t)\geqslant 0.5} \rho_1 \mathrm{d}V, \tag{49a}$$

$$m_2(t) = \int_{\Omega,\phi(t)<0.5} \rho_2 \mathrm{d}V, \tag{49b}$$

Let $M_1 = m_1(t)/m_1(0)$, $M_2 = m_2(t)/m_2(0)$, Fig. 8 gives the M_1-t and M_2-t curves. It can be seen that after stabilization, the mass of each phase obtained by the incompressible model[18] has a large deviation from the initial value, with a relative error of 3.53%, while the mass deviation of the quasi-incompressible model is small, with a relative error of only 0.67%.

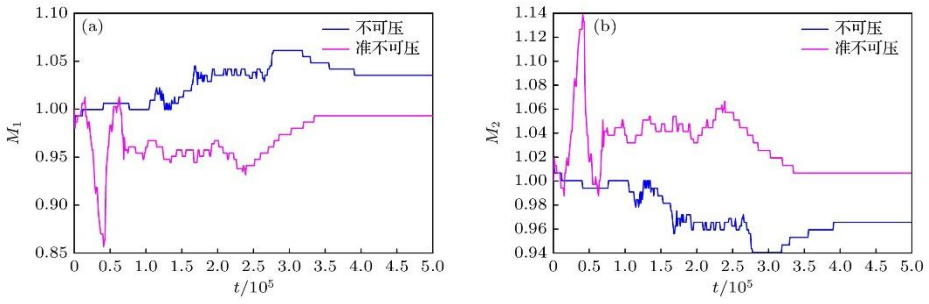

Figure 8. Variation of single-phase mass over time.

5. Conclusion

Based on the quasi-incompressible phase-field theory, a two-phase LBE model is proposed in this paper, which can achieve well-balanced state on the discrete scale. The flat interface problem and the staionary droplet problem are simulated and compared with the quasi-incompressible phase-field YG-LBE model[3] without well-balanced property. The results show that the proposed model eliminates the spurious velocity to machine accuracy and obtains an almost constant chemical potential, which proves the well-balanced performance of the current model. The effects of different surface tension forms and different viscosity mixing rules are also compared in the simulation of stationary droplet problem. The results show that the form of surface tension expressed by (45b) does not guarantee that the chemical potential is constant and the well-balanced state cannot be achieved; Different viscosity mixing rules have no significant effect on the model when simulating static problems. Layered Poiseuille flow is further simulated, and the effects of different viscosity mixing rules are compared. The results show that more accurate results can be obtained by using the step mixing rule to calculate the mixing viscosity. Layered Poiseuille flow with different viscosity ratios is also simulated, and the results are in good agreement with the analytical solution, which proves the accuracy of the current model in simulating dynamic problems and problems with large viscosity ratios. In addition, a two-phase separation problem is simulated to show the difference between the quasi-incompressible model and the incompressible model, and to prove that the proposed model can ensure local mass conservation. In a word, the well-balanced two-phase LBE model proposed in this paper solves the spurious velocity problem of the original model, and at the same time, it can ensure the local mass conservation.

References

[1] Guo Z L, Shu C 2013 Lattice Boltzmann Method and its Application in Engineering (Vol. 3) (Singapore: World Scientific Publishing

[2] Huang H B, Sukop M, Lu X Y 2015 Multiphase Lattice Boltzmann Methods: Theory and Application (Hoboken, NJ: Wiley-Blackwell

[3] Yang K, Guo Z L 2016 Phys. Rev. E 93 043303

[4] Zhang C H, Guo Z L, Liang H 2021 Int. J. Numer. Methods Fluids 93 2225

[5] Connington K, Lee T 2012 J. Mech. Sci. Technol. 26 3857

[6] Gong J M, Oshima N, Tabe Y 2019 Comput. Math. Appl. 78 1166

[7] Huang H B, Krafczyk M, Lu X Y 2011 Phys. Rev. E 84 046710

[8] Zhai Q L, Zheng L, Zheng S 2017 Phys. Rev. E 95 023313

[9] Siebert D, Philippi P, Mattila K 2014 Phys. Rev. E 90 053310

[10] Cristea A, Sofonea V 2003 Int. J. Mod. Phys. C 14 1251

[11] Wagner A J 2003 Int. J. Mod. Phys. B 17 193

[12] Shan X 2006 Phys. Rev. E 73 047701

[13] Sbragaglia M, Benzi R, Biferale L, Succi S, Sugiyama K, Toschi F 2007 Phys. Rev. E 75 026702

[14] Guo Z L, Zheng C G, Shi B C 2011 Phys. Rev. E 83 036707

[15] Guo Z L 2021 Phys. Fluids 33 031709

[16] Zhang C H, Guo Z L, Wang L P 2022 Phys. Fluids 34 012110

[17] Zheng L, Zheng S, Zhai Q L 2021 Phys. Fluids 33 092102

[18] Ju L, Liu P Y, Yan B C, Bao J, Sun S Y, Guo Z L 2023 arXiv: 2311.10827v1 [physics. flu-dyn]

[19] Lowengrub J, Truskinovsky L 1998 Proc. R. Soc. London, Ser. A 454 2617

[20] Shen J, Yang X F, Wang Q 2013 Commun. Comput. Phys. 13 1045

[21] Jacqmin D 1999 Commun. Comput. Phys. 155 96

[22] Deng B, Shi B C, Wang G C 2005 Chin. Phys. Lett. 22 267